

Probing the Fermi surface with Quantum Oscillation Measurements in the Dirac semimetal TaNiTe₅

Maximilian Daschner,^{1,2,*} Bruno Gudac,³ Mario Novak,³
Cheng Liu,¹ F. Malte Grosche,¹ and Ivan Kokanović^{3,1,†}

¹*Cavendish Laboratory, University of Cambridge, Cambridge CB3 0HE, United Kingdom*

²*Fakultät für Physik, Ludwig-Maximilians-Universität, München, Germany*

³*Department of Physics, Faculty of Science, University of Zagreb, Zagreb, Croatia*

We report a detailed investigation of the Fermi surface in the layered Dirac semimetal TaNiTe₅. We probed the magnetization, magnetic torque and magnetoresistance in high-quality single crystals. Pronounced Shubnikov - de Haas (SdH) and de Haas - van Alphen (dHvA) oscillations are observed in magnetic fields above 3 T and at temperatures of up to 22 K. Multiple fundamental frequencies and light effective quasiparticle masses are obtained by fast Fourier transformation (FFT) and Lifshitz-Kosevich (LK) formula fits. The high resolution of the low-temperature FFT spectra allows us to investigate individual peaks in detail for the magnetic fields applied along all three crystallographic axes and the planes in between. Our investigation can confirm the density functional theory (DFT) calculated band structure and its corresponding Fermi surface.

I. INTRODUCTION

Topological semimetals represent a new class of quantum materials hosting Dirac [1–4] or Weyl fermions [5–13], in which the valence and conduction bands touch and form nodal points. Furthermore, Dirac nodal-lines in which Dirac cones form lines in reciprocal space lead to the more general concept of nodal-line semimetals (NLSMs) [14–20]. NLSMs usually occur in three-dimensional materials where they hold more symmetries such as mirror and nonsymmorphic symmetries that protect the Dirac band touching structures against spin-orbit coupling (SOC) [16, 19]. Evidence for robust Dirac nodal lines in (quasi) one-dimensional materials has been missing until recently when they were reported in the exfoliatable, in-plane anisotropic nonmagnetic semimetal TaNiTe₅ by combining angle-resolved photoemission spectroscopy (ARPES) and density functional theory (DFT) calculations [21]. Quantum oscillation studies have reported evidence for Fermi surface pockets with nontrivial Berry phase in TaNiTe₅, and highly anisotropic properties were shown in magnetization and transport measurements [22–24]. These previous studies were performed for magnetic fields applied parallel to the crystallographic *a* and *b* axes. However, a system-

atic study of quantum oscillations for magnetic fields parallel to the crystallographic *c*-axis or in any of the planes perpendicular to the *a* or *b* axes remains absent. Here, we report a detailed investigation of the Fermi surface in TaNiTe₅ single crystals through magnetization, magnetic torque and magnetoresistance measurements for magnetic fields of up to 14 T along all three principal axes and a rotational study in all three planes. We observed pronounced de Haas - van Alphen (dHvA) and Shubnikov - de Haas (SdH) oscillations with multiple frequencies at temperatures below 22 K and magnetic fields above 3 T. The observed quantum oscillation frequencies in these crystals closely agree with each other, evidencing the same electronic structure. Changing the magnetic field direction results in a clear change of the oscillation frequencies, indicating anisotropic Fermi surface pockets. By analyzing the SdH and dHvA quantum oscillations, multiple fundamental frequencies, small effective masses, low Dingle temperatures, and high mobility of charge carriers are obtained. The high resolution of the low-temperature FFT spectra in the observed magnetization and magnetoresistance data allows us to investigate individual peaks in detail. Our results shed light on the electronic properties of the Dirac semimetal TaNiTe₅ and serve as a basis for the study of low-dimensional quantum materials and their topological properties.

* maximilian.daschner@lmu.de

† kivan@phy.hr

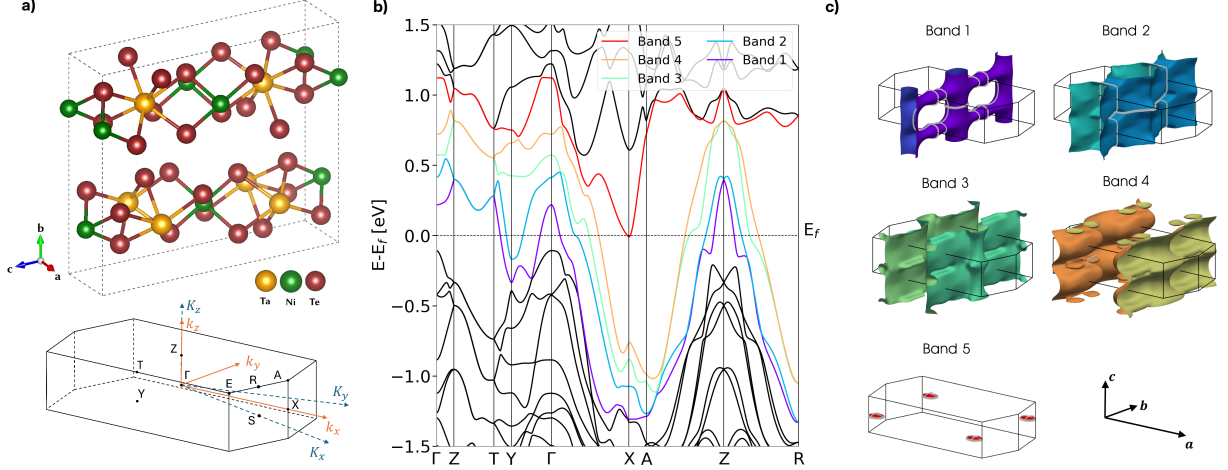


Figure 1. a) Unit cell and first Brillouin zone in TaNiTe₅. In the Brillouin zone, k_x , k_y , and k_z point in conventional unit cell vector directions which go through high-symmetry points X, Y and Z and align with the crystallographic axes a , b , and c , respectively, while K_x , K_y , and K_z are the reciprocal lattice vectors that represent the periodicity of the Brillouin zone. b) Band structure including spin-orbit coupling along high-symmetry lines. c) Fermi sheets for TaNiTe₅ with the Fermi level shifted to lower energies by approximately 20 meV. Extremal orbits are shown for the magnetic field along a , b and c as gray lines in the first Brillouin zone.

II. EXPERIMENTAL METHODS

The TaNiTe₅ crystals were synthesized by the self-flux method [23, 25]. The mixture at a molar ratio of Ta:Ni:Te = 1:1:10 was loaded into an alumina crucible and sealed inside a quartz tube in high vacuum. The mixture was then heated to 700 °C over the course of four days and slowly cooled to 500 °C within a week. The resulting single crystals have an orthorhombic layered structure with the space group Cmc_m (No. 63) [25]. The structure features one-dimensional (1D) NiTe₂ chains along the crystallographic a -axis, which form a quasi-2D layer by linking chains of Ta atoms along the c -axis as can be seen in Figure 1 a). The lattice constants are inferred from powder X-ray diffraction (XRD) data with $a = 3.657$ Å, $b = 13.183$ Å, and $c = 15.119$ Å. The peaks of the single-crystal XRD pattern showed no trace of an impurity phase, indicating high crystalline quality (see Appendix A). The crystals grow in the shape of flat needles along the a -axis. Magnetization measurements in two crystals with masses of 25 mg and 27.4 mg were carried out using a 14 Tesla Quantum Design Physical Property Measurement System (PPMS) with VSM option. The magnetoresistance was measured using standard AC lock-in techniques in a

9 Tesla PPMS. We have also performed magnetic torque measurements on two crystals in magnetic fields of up to 9 T and 13 T for the angle-dependent measurement in the a - b plane and the b - c plane, respectively. These were carried out in the aforementioned 9 Tesla PPMS, and a customized 13 Tesla Oxford Instruments cryostat. The crystals were mounted on custom-made piezoresistive cantilevers and placed on a rotating platform.

III. AB INITIO CALCULATIONS

To gain insights into the electronic structure of TaNiTe₅, we have performed density functional theory (DFT) calculations using the full-potential linearized augmented plane wave method implemented in the Wien2k package [26]. The PBE-GGA exchange-correlation functional [27] was chosen here. The atomic sphere radii (muffin-tin radii) were chosen as $R_{mt} = 2.5$ a.u. for the Ta and Ni atoms, and $R_{mt} = 2.43$ a.u. for all Te atoms. The plane-wave cut-off parameter was chosen as $R_{mt}K_{max} = 8$, where R_{mt} is the smallest atomic sphere radius in the unit cell and K_{max} is the magnitude of the largest k-vector. Calculations were performed on a $59 \times 59 \times 13$ k-point mesh in

the full Brillouin zone for the band structure calculations shown here. Figure 1 b) illustrates the resulting band structure including spin-orbit coupling (SOC) with its respective Fermi sheets shown in Figure 1 c). The Fermi sheets for each band also include extremal areas for magnetic fields aligned with the three crystallographic axes a , b or c .

From Figure 1 b) it can be seen that linearly dispersing bands appear in pairs along the A-Z-R high-symmetry line, forming Type-I Dirac cones in Z, and Type-II Dirac cones in R as the bands maintain their spin-degeneracy. Similar to the material family members TaXTe₅ (X = Pd, Pt), TaNiTe₅ also hosts a four-fold degenerate nodal-line along Z-T, with linear dispersion along Γ -Z and T-Y. Symmetry considerations [1, 28] performed in the literature for materials that crystallise in the symmetry group Cmcm (63), e.g. TaNiTe₅ [21], TaPtTe₅ [29], LaNiGa₂ [30], and Th₂BC₂ [31] show protection of such nodal-lines. Their energetic location is around 200 meV above the Fermi level, making it unlikely for them to influence our obtained experimental results [22, 32, 33].

IV. THEORY

In metals and semimetals, oscillations in various physical quantities in magnetic field are well described by the grand thermodynamical potential given by the Lifshitz-Kosevich (LK) formula [34]:

$$\Omega = \sum_i C_i B^{\frac{5}{2}} R_T R_D \cos\left(2\pi\left(\frac{F_i}{B} - \frac{1}{2} + \phi\right)\right) \quad (1)$$

where the sum is over all orbits i along a Fermi sheet, and we assume only one harmonic for simplicity. B is the magnetic field, C_i is a B -independent constant, F is the dHvA frequency of the oscillations, which can be related to the extremal area A of the individual pocket via the Onsager relation $F = A(\phi_0/2\pi^2)$, where ϕ_0 is the magnetic flux quantum [34], and m^* is the quasi-particle effective mass. We also include a phase shift $\phi = \phi_B/2\pi + \delta$ where ϕ_B is the Berry phase, and δ is an additional phase shift depending on the dimensionality of the Fermi surfaces, i.e. $\delta = 0$ for 2D Fermi surfaces, and $\delta = \pm 1/8$ for 3D Fermi surfaces ($-1/8$ for the electron-like and $1/8$ for the hole-like). $R_T = X/\sinh(X)$ with

$X = 2\pi^2 k_B m^* T / (\hbar e B)$ is the temperature damping factor, while $R_D = \exp(-XT_D/T)$ is the Dingle damping factor which accounts for finite particle lifetime.

The mean free path l can be approximated under the assumption of a spherical Fermi surface as

$$l = \frac{\sqrt{2e\hbar^3 F}}{2\pi m^* k_B T_D} \quad (2)$$

while quantum relaxation time and quantum mobility are defined as $\tau_q = \hbar/(4\pi^2 k_B T_D)$ and $\mu_q = e\tau_q/m^*$, respectively.

Shubnikov - de Haas oscillations in the magnetoresistance are proportional to Equation 1, while de Haas - van Alphen oscillations in the magnetization can be derived via $M_{\parallel} = -\left(\frac{d\Omega}{dB}\right)$. Oscillations in the magnetic torque are then given by

$$\tau = \mathbf{M}_{\perp} \times \mathbf{B} \quad (3)$$

where the perpendicular magnetization is given by

$$\mathbf{M}_{\perp} = -\frac{1}{F} \frac{dF}{d\theta} \cdot \mathbf{M}_{\parallel} \quad (4)$$

Using this formalism, we will analyze the magnetization, magnetic torque and magnetoresistance data obtained for TaNiTe₅ in what follows.

V. EXPERIMENTAL RESULTS

A. Magnetization

Figure 2 a) shows a series of magnetization measurements in TaNiTe₅ at a temperature of 1.8 K, with magnetic fields applied along the crystallographic a , b , and c axes. TaNiTe₅ exhibits large dHvA quantum oscillations with multiple frequencies superimposed on different linear diamagnetic backgrounds. By changing the direction of the magnetic field from $\mathbf{B} \parallel b$ to $\mathbf{B} \parallel a$, and to $\mathbf{B} \parallel c$, the oscillation components are gradually suppressed, illustrating the anisotropic electronic properties of this material with an anisotropic magnetic susceptibility ratio of $\chi_a:\chi_c:\chi_b=3.3:4.5:6.3$ at 1.8 K.

In Figure 2 b), we have performed a FFT analysis of the isothermal magnetization data shown in Figure 2 a). Several clearly resolved peaks are visible for the magnetic field parallel to each crystallographic axis, which we label with greek letters.

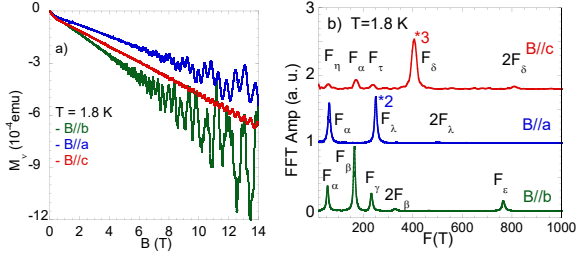


Figure 2. a) Magnetization of a layered TaNiTe₅ single crystal with a mass of 25.6 mg at a temperature of 1.8 K. The magnetic field is applied parallel to the crystallographic *b*, *a*, and *c* axes, respectively. The curves show an interpolation of data points with a few data points highlighted for **B**||*c* (red circle), **B**||*a* (blue square), and **B**||*b* (green triangle). b) FFT spectra of the dHvA oscillations in the isothermal magnetization data extracted after subtracting the diamagnetic backgrounds shown in a). The FFT amplitudes of the spectra have been generated from the magnetization data between 4 T and 14 T and are shifted vertically for clarity.

The observed frequencies (*F*) in the FFT spectra are related to the extremal area through the Onsager relation. Frequencies we found here are consistent with the literature [22–24].

The raw data for the magnetization measurements along all three crystallographic axes at different temperatures is given in Appendix B. The diamagnetic background in this data was subtracted with a polynomial, and the resulting oscillatory part was fast Fourier transformed as illustrated in Figure 3. From the FFT amplitudes, the effective mass m^* can be extracted using the temperature-damping term R_T as shown in the insets on the right. With the fitted effective mass as a known parameter, we have further fitted the oscillation pattern at 1.8 K to the LK formula, from which the Dingle temperature T_D , quantum mobility μ_q , and a phase shift ϕ of the Fermi pockets are extracted and listed in Table I. Only two orbits were considered in each fit at a time. After subtracting the corresponding oscillation pattern, we performed another two-band LK formula fit to the residual data (see Appendix C). Note, that for **B**||*c* the amplitude was too low to obtain reliable values for the phase shift ϕ for F_η and F_τ . The fitted Dingle temperature T_D , the quantum relaxation time τ_q and quantum mobility μ_q for all frequencies are also included in Table I.

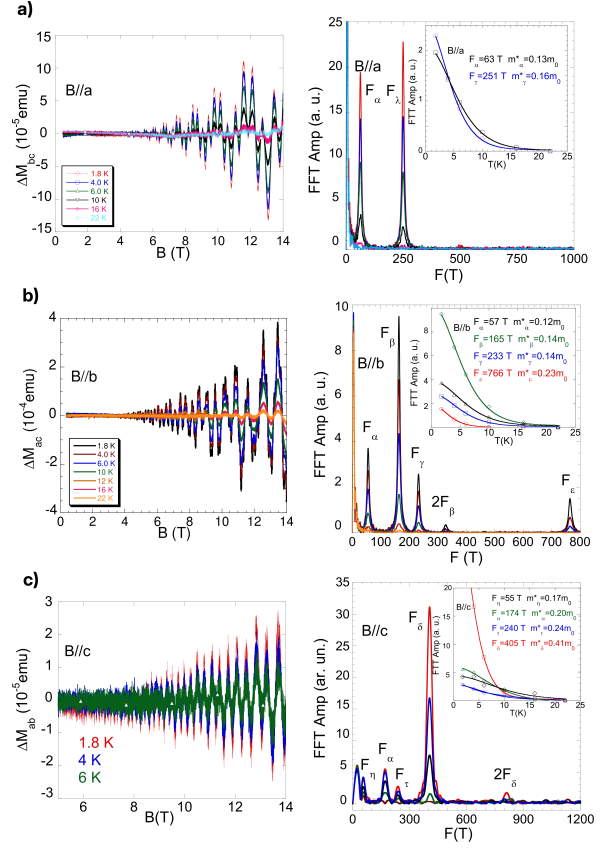


Figure 3. Analysis of dHvA oscillations with a) **B**||*a*, b) **B**||*b*, and c) **B**||*c*. Left: The oscillatory components of the isothermal magnetization ΔM after subtracting the diamagnetic background at various temperatures. Right: The corresponding FFT amplitude of the spectra has been generated from data between 4 T and 14 T. The inset shows the fits of the temperature damping factor R_T in the LK formula to the FFT amplitudes.

To probe the morphology of the Fermi surface, we furthermore carried out angle-dependent quantum oscillation measurements in the magnetization with the applied magnetic field in the crystallographic *a*-*c* plane. The background subtracted raw data for four angles in that plane including its respective FFT is shown Figure 4.

With increasing angle θ from 0° to 90° , the oscillation components are suppressed gradually. It can be seen from Figure 5 a) that with increasing the angle θ , the oscillation frequency F_α changes only slightly from 63 T ($\theta = 0^\circ$) to 73 T

Table I. Extracted properties from de Haas van Alphen oscillations in the magnetization.

	F (T)	A_F (\AA^{-2})	m^* (m_e)	T_D (K)	τ_q (10^{-14} s)	μ_q (m^2/Vs)	l (nm)	ϕ (π)
B b								
F_α	56.8(3)	0.00542(3)	0.12(1)	15.5(3)	7.8(2)	0.11(1)	31(3)	0.64(5)
F_β	164.7(3)	0.01572(3)	0.14(1)	12.6(3)	9.6(2)	0.121(9)	56(4)	1.14(4)
F_γ	233.1(3)	0.02225(3)	0.14(2)	12.5(5)	9.7(4)	0.12(2)	70(10)	0.98(3)
F_ε	766.0(5)	0.07312(5)	0.23(2)	12.3(5)	9.9(4)	0.076(7)	76(7)	0.81(4)
B c								
F_η	55.3(3)	0.00528(3)	0.17(2)	28.6(3)	4.25(4)	0.044(5)	12(1)	-
F_α	173.8(4)	0.01659(4)	0.20(2)	13.4(3)	9.1(2)	0.080(8)	38(4)	1.03(3)
F_τ	240.0(4)	0.02291(4)	0.24(3)	13.6(4)	8.9(3)	0.066(8)	37(5)	-
F_δ	405.2(4)	0.03868(4)	0.41(2)	4.7(3)	26(2)	0.111(9)	81(7)	1.30(3)
B a								
F_α	63.0(3)	0.00601(3)	0.13(1)	15.8(3)	7.7(1)	0.104(8)	30(2)	1.10(5)
F_λ	251.0(4)	0.02396(4)	0.16(1)	10.8(3)	11.3(3)	0.124(8)	71(5)	1.01(5)
B a \rightarrow B c ($\theta = 15^\circ$)								
F_α	64.0(2)	0.00611(2)	0.19(1)	12.9(5)	9.4(4)	0.087(6)	25(2)	0.62(3)
F_λ	254.0(4)	0.02425(4)	0.24(1)	8.7(3)	14.0(5)	0.102(6)	59(3)	0.95(4)
B a \rightarrow B c ($\theta = 35^\circ$)								
F_α	73.0(2)	0.00697(2)	0.18(1)	12.4(4)	9.8(3)	0.096(6)	30(2)	0.61(3)
F_λ	286.0(4)	0.02730(4)	0.26(1)	12.5(4)	9.7(3)	0.066(3)	40(2)	1.28(5)

($\theta = 35^\circ$), before increasing steeply to 173.8 T at $\theta = 90^\circ$, indicating a 3D elliptical Fermi pocket. This motivates fitting the angle dependence of the F_α pocket with the 3D ellipsoid model (thick red line) described in [35]. On the other hand, the frequency F_λ increases from 251 T ($\theta = 0^\circ$) to 286 T

($\theta = 35^\circ$), and disappears for the angles larger than ($\theta = 35^\circ$). This motivates the model of a 2-dimensional Fermi sheet (FS), and hence we fit the data with $F_{2D}/\cos(\theta) + F_{3D}$ [36] (thick blue line), which includes both 2D and isotropic 3D FS components. We find the ratio $F_{2D}/F_{3D} \approx 1.65$, and conclude that the dimensionality of the FS associated with F_λ is a mixture of 2D and 3D character where the former dominates. We also include the results from DFT calculations in Figure 5 a) (thin lines) which seem to agree well with the experimental findings after shifting the Fermi energy by 20 meV. Particularly bands 2 and 5 (see Figure 1) can explain the presence of the branches F_λ and F_α , respectively, while band 1 seems to overestimate F_δ . The frequencies $F_\tau=240$ T and $F_\eta=55.3$ T for **B||c** are two new frequencies, which have not been reported in the literature thus far. With the strong anisotropy of the crystal, the oscillatory signal is the weakest along the *c* direction, and more measurements are necessary to conclusively confirm the existence of these two additional frequencies. Effective masses and other quantities

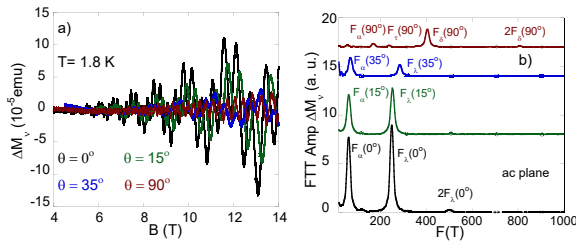


Figure 4. a) The magnetic field-dependent oscillatory components of the magnetization after subtracting the linear diamagnetic background at different angles in the *a-c* plane at $T = 1.8$ K. b) The corresponding FFT spectra for different angles. The angle θ in the *a-c* plane is defined as the angle between the applied magnetic field and the *a*-axis.

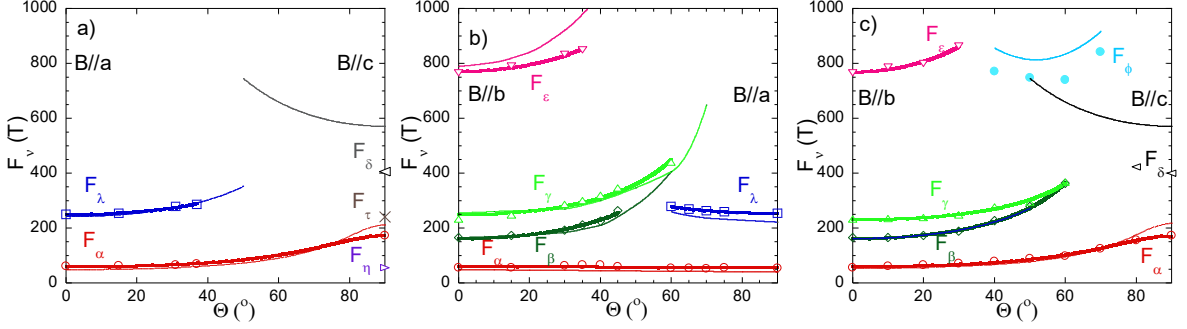


Figure 5. The angular dependence of the oscillation frequencies. The F_α branch was fitted with the ellipsoid model, while all other branches were fitted with the $F_{2D}/\cos(\theta) + F_{3D}$ model described in the main text and illustrated by thick lines. DFT calculations are included via thin lines. a) Magnetization in the a - c plane. b) Magnetic torque in the a - b plane. c) Magnetic torque in the b - c plane.

were extracted for data points in the a - c plane and are included in Table I. Note that an additional data point at around 30° is included in Figure 5 a), but due to the lack of a temperature-dependent study, only its frequency could be determined.

B. Magnetic Torque

To obtain a better understanding of the morphology of the Fermi surface, we carried out angle-dependent quantum oscillation measurements in the magnetic torque with the magnetic field in the a - b plane up to 9 T and in the b - c plane up to 13 T. An analysis is shown in Appendix D, and the results are summarized Figure 5 b) and Figure 5 c). Again, the oscillation frequency F_α can be well fitted with the 3D ellipsoid model. In the a - b plane, F_λ decreases from 276 T ($\theta = 60^\circ$) to 251 T ($\theta = 90^\circ$), while disappearing for the angles smaller than $\theta = 60^\circ$. This dependence is fitted by $F_{2D}/\cos(\theta) + F_{3D}$, and results in a ratio of $F_{2D}/F_{3D} \approx 1.9$. With increasing the angle θ , the highest frequency branch F_ϵ continues to increase until it disappears above $\theta = 35^\circ$. For F_β , F_γ and F_ϵ we find ratios of $F_{2D}/F_{3D} \approx 16.5$, $F_{2D}/F_{3D} \approx 4.1$ and $F_{2D}/F_{3D} \approx 0.9$, respectively. Comparing these results to the rotation study in magnetic torque in the a - b plane performed by Z. Chen et al. [23], we have observed agreement for the low frequency branch F_α , both in magnitude and the angle-dependence. Z. Chen et al. [23] also report oscillation data for the electron-branch F_λ and lower hole-branch F_β , although they mis-

takenly conclude that these frequencies must arise from the same Fermi surface. The upper hole-branch F_γ was not reported at all. Our DFT analysis shows that the branches F_β and F_γ arise from band 1, while F_λ arises from band 2 as noted before. Furthermore, Z. Chen et al. [23] also report the hole-branch F_ϵ and an additional branch with similar angular dependence with a 150 T larger frequency. However, both results disagree with the authors' own Shubnikov-de Haas study, which finds only one instead of two frequencies at a value more consistent with our measurements. We find that F_ϵ originates from the Fermi sheet in band 2.

The angle dependence of the oscillation frequencies from the torque measurements in the b - c plane are shown in Figure 5 c). The frequency branches show similar behavior as in the a - b plane with ratios of $F_{2D}/F_{3D} \approx 17.2$ for the F_β pocket, $F_{2D}/F_{3D} \approx 1.4$ for the F_γ pocket and $F_{2D}/F_{3D} \approx 3.5$ for the F_ϵ pocket. No attempt was made to fit F_ϕ , but regarding DFT calculations we find that it most likely arises from band 1.

C. Magnetoresistance

Figure 6 a) shows the magnetoresistance data with the magnetic field parallel to the b -axis and the applied current parallel to the a -axis. The oscillations in the magnetoresistance shown here are significantly more pronounced than what has been reported in recent works [22, 23], in which quantum oscillations in the magnetoresistance of TaNiTe_5 were only observed at magnetic fields of up to

Table II. Extracted properties from Shubnikov de Haas oscillations in the resistivity with $\mathbf{B} \parallel b$ and $\mathbf{I} \parallel a$.

	F (T)	A_F (\AA^{-2})	m^* (m_e)	T_D (K)	τ_q (10^{-14} s)	μ_q (m^2/Vs)	l (nm)	ϕ (π)
F_α	53.0(3)	0.00506(3)	0.14(2)	12.9(4)	9.4(3)	0.12(2)	31(5)	1.03(3)
F_β	163.0(4)	0.01556(4)	0.23(1)	14.7(3)	8.3(2)	0.063(3)	29(1)	1.05(4)
F_γ	233(3)	0.0222(3)	0.23(3)	-	-	-	-	-
F_ϵ	766(5)	-	-	-	-	-	-	-

50T. The strong quantum oscillations shown here indicate a possible new topological phenomenon, however a model based on classical phenomena can fully explain the origin of this amplification of quantum oscillations as described in more detail in [37].

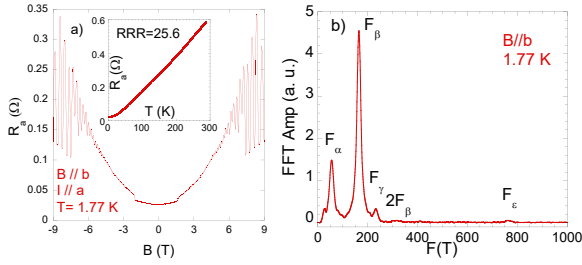


Figure 6. a) Magnetic field dependent resistance R_a with the current applied along the a -axis, and the magnetic field parallel to the b -axis. The inset shows the temperature dependence of the resistance R_a at 0 T. b) The FFT spectrum of ΔR_a generated in the magnetic field range from 3 to 9 T.

The inset to Figure 6 a) shows the temperature dependence of the resistance R_a displaying a typical metallic behavior. The resistance follows a T -linear dependence from 280K to 50K and then a cross-over to a quadratic T -dependence indicating Fermi liquid behavior below 50K. The residual resistance ratio is measured as $RRR = 25.6$. Moreover, the quasi-1D transport behavior with a resistance ratio of $\rho_a:\rho_c = 1:4$ at 2 K has been obtained and is consistent with previous reports [22, 23]. Using this data, we performed a fast Fourier transform in the magnetic field range between 3 T and 9 T as shown in Figure 6 b).

Similar to the magnetization data, magnetoresistance data in the temperature range 1.77 K - 20 K allows us to extract the effective mass, and other parameters (see Appendix F). Given m^* , the

Dingle temperature T_D , quantum mobility μ_q , and the phase shift ϕ_B of the Fermi pockets are extracted at $T = 1.77$ K, and summarized Table II. The resolution of the γ and ϵ pockets is too low to extract most parameters other than the frequencies, and the effective mass for the γ pocket.

VI. CONCLUSIONS

We performed high-resolution measurements of de Haas - van Alphen and Shubnikov - de Haas quantum oscillations in layered TaNiTe_5 along all three crystallographic axes and the planes in between. The obtained fundamental frequencies in the FFT spectra resulting from dHvA measurements are consistent with those found in SdH measurements when the magnetic field is applied parallel to the b -axis. Furthermore, quantum oscillation measurements in the magnetization, magnetic torque and the magnetoresistance are consistent with previously reported values in the literature and density functional theory calculations performed here. Our rotation studies allow us to map out the morphology of the Fermi surface in this material, and we discovered new fundamental frequencies that had been absent from the literature thus far.

ACKNOWLEDGMENTS

This work was supported by the Croatian Science Foundation under the project IP 2018 01 8912 and by the EPSRC of the UK under grant EP/X011992/1. This work was also supported by the Henry Royce Institute for advanced materials through the Equipment Access Scheme enabling access to the Magnetic Property Measurement System (MPMS) at Cambridge; Cambridge Royce facilities grant EP/P024947/1 and Sir Henry Royce Institute - recurrent grant EP/R00661X/1)

-
- [1] S. M. Young and C. L. Kane, Physical review letters **115**, 126803 (2015).
 - [2] M. Yan, H. Huang, K. Zhang, E. Wang, W. Yao, K. Deng, G. Wan, H. Zhang, M. Arita, H. Yang, *et al.*, Nature communications **8**, 257 (2017).
 - [3] J. Xiong, S. K. Kushwaha, T. Liang, J. W. Krizan, M. Hirschberger, W. Wang, R. J. Cava, and N. P. Ong, Science **350**, 413 (2015).
 - [4] S. Borisenko, Q. Gibson, D. Evtushinsky, V. Zabolotnyy, B. Buchner, and R. J. Cava, Phys. Rev. Lett. **113**, 027603 (2014).
 - [5] S. M. Huang, S. Y. Xu, I. Belopolski, C. C. Lee, G. Chang, B. Wang, N. Alidoust, G. Bian, M. Neupane, C. Zhang, S. Jia, A. Bansil, H. Lin, and M. Z. Hasan, Nat. Commun. **6**, 7373 (2015).
 - [6] A. A. Soluyanov, D. Gresch, Z. Wang, Q. Wu, M. Troyer, X. Dai, and B. A. Bernevig, Nature (London) **527**, 495 (2015).
 - [7] H. Weng, C. Fang, Z. Fang, B. A. Bernevig, and X. Dai, Phys. Rev. X **5**, 011029 (2015).
 - [8] B. Q. Lv, N. Xu, H. M. Weng, J. Z. Ma, P. Richard, X. C. Huang, L. X. Zhao, G. F. Chen, C. E. Matt, F. Bisti, V. N. Strocov, J. Mesot, Z. Fang, X. Dai, T. Qian, M. Shi, and H. Ding, Nat. Phys. **11**, 724 (2015).
 - [9] S.-Y. Xu, N. Alidoust, I. Belopolski, Z. Yuan, G. Bian, T.-R. Chang, H. Zheng, V. N. Strocov, D. S. Sanchez, G. Chang, *et al.*, Nature Physics **11**, 748 (2015).
 - [10] S.-Y. Xu, I. Belopolski, N. Alidoust, M. Neupane, G. Bian, C. Zhang, R. Sankar, G. Chang, Z. Yuan, C.-C. Lee, *et al.*, Science **349**, 613 (2015).
 - [11] S.-Y. Xu, C. Liu, S. K. Kushwaha, R. Sankar, J. W. Krizan, I. Belopolski, M. Neupane, G. Bian, N. Alidoust, T.-R. Chang, H.-T. Jeng, C.-Y. Huang, W.-F. Tsai, H. Lin, P. P. Shibayev, F.-C. Chou, R. J. Cava, and M. Z. Hasan, Science **347**, 294 (2015).
 - [12] L. X. Yang, Z. K. Liu, Y. Sun, H. Peng, H. F. Yang, T. Zhang, B. Zhou, Y. Zhang, Y. F. Guo, M. Rahn, D. Prabhakaran, Z. Hussain, S. K. Mo, C. Felser, B. Yan, and Y. L. Chen, Nat. Phys. **11**, 728 (2015).
 - [13] Z. K. Liu, L. X. Yang, Y. Sun, T. Zhang, H. Peng, H. F. Yang, C. Chen, Y. Zhang, Y. F. Guo, D. Prabhakaran, M. Schmidt, Z. Hussain, S. K. Mo, C. Felser, B. Yan, and Y. L. Chen, Nat. Mater. **15**, 27 (2016).
 - [14] C. Fang, H. Weng, X. Dai, and Z. Fang, Chin. Phys. B **25**, 117106 (2016).
 - [15] R. Yu, Z. Fang, X. Dai, and H. Weng, Front. Phys. **12**, 127202 (2017).
 - [16] L. M. Schoop, M. N. Ali, C. Strasser, A. Topp, A. Varykhalov, D. Marchenko, V. Duppel, S. S. Parkin, B. V. Lotsch, and C. R. Ast, Nat. Commun. **7**, 11696 (2016).
 - [17] C. Fang, Y. Chen, H.-Y. Kee, and L. Fu, Phys. Rev. B **92**, 081201(R) (2015).
 - [18] T. Bzdusek, Q. Wu, A. Ruegg, M. Sigrist, and A. A. Soluyanov, Nature (London) **538**, 75 (2016).
 - [19] S.-Y. Yang, H. Yang, E. Derunova, S. S. P. Parkin, B. Yan, and M. N. Ali, Adv. Phys.: X **3**, 1414631 (2018).
 - [20] J. Hu, Z. Tang, J. Liu, X. Liu, Y. Zhu, D. Graf, K. Myhro, S. Tran, C. N. Lau, J. Wei, and Z. Mao, Phys. Rev. Lett. **117**, 016602 (2016).
 - [21] Z. Hao, W. Chen, Y. Wang, J. Li, X.-M. Ma, Y.-J. Hao, R. Lu, Z. Shen, Z. Jiang, W. Liu, *et al.*, Physical Review B **104**, 115158 (2021).
 - [22] C. Xu, Y. Liu, P. Cai, B. Li, W. Jiao, Y. Li, J. Zhang, W. Zhou, B. Qian, X. Jiang, *et al.*, The Journal of Physical Chemistry Letters **11**, 7782 (2020).
 - [23] Z. Chen, M. Wu, Y. Zhang, J. Zhang, Y. Nie, Y. Qin, Y. Han, C. Xi, S. Ma, X. Kan, J. Zhou, X. Yang, X. Zhu, W. Ning, and M. Tian, Phys. Rev. B **103**, 035105 (2021).
 - [24] R. Ye, T. Gao, H. Li, X. Liang, and G. Cao, AIP Advances **12**, 045104 (2022).
 - [25] C. E. W. Liimatta and J. A. Ibers, J. Solid State Chem. **78**, 7 (1989).
 - [26] P. Blaha, K. Schwarz, G. K. Madsen, D. Kvasnicka, J. Luitz, *et al.*, An augmented plane wave+local orbitals program for calculating crystal properties **60** (2001).
 - [27] J. P. Perdew, K. Burke, and M. Ernzerhof, Phys. Rev. Lett. **77**, 3865 (1996).
 - [28] S. M. Young, S. Zaheer, J. C. Teo, C. L. Kane, E. J. Mele, and A. M. Rappe, Physical review letters **108**, 140405 (2012).
 - [29] S. Xiao, W.-H. Jiao, Y. Lin, Q. Jiang, X. Yang, Y. He, Z. Jiang, Y. Yang, Z. Liu, M. Ye, *et al.*, Physical Review B **105**, 195145 (2022).
 - [30] J. R. Badger, Y. Quan, M. C. Staab, S. Sumita, A. Rossi, K. P. Devlin, K. Neubauer, D. S. Shulman, J. C. Fetting, P. Klavins, *et al.*, Communications Physics **5**, 22 (2022).
 - [31] M. Wang, Y. Wang, Z. Yang, J. Fan, B. Zheng, R. Wang, and X. Wu, Physical Review B **105**, 174309 (2022).
 - [32] W.-H. Jiao, X.-M. Xie, Y. Liu, X. Xu, B. Li, C.-Q. Xu, J.-Y. Liu, W. Zhou, Y.-K. Li, H.-Y. Yang, S. Jiang, Y. Luo, Z.-W. Zhu, and G.-H. Cao, Phys. Rev. B **102**, 075141 (2020).

- [33] W.-H. Jiao, S. Xiao, B. Li, C. Xu, X.-M. Xie, H.-Q. Qiu, X. Xu, Y. Liu, S.-J. Song, W. Zhou, H.-F. Zhai, X. Ke, S. He, and G.-H. Cao, Phys. Rev. B **103**, 125150 (2021).
- [34] D. Shoenberg, *Magnetic oscillations in metals* (Cambridge university press, 1984).
- [35] P. Rourke and S. Julian, Computer Physics Communications **183**, 324 (2012).
- [36] J. Hu, Z. Tang, J. Liu, Y. Zhu, J. Wei, and Z. Mao, Physical Review B **96**, 045127 (2017).
- [37] M. Daschner, I. Kokanović, and F. M. Grosche, arXiv preprint arXiv:2507.02612 (2025).

Appendix A: Methods

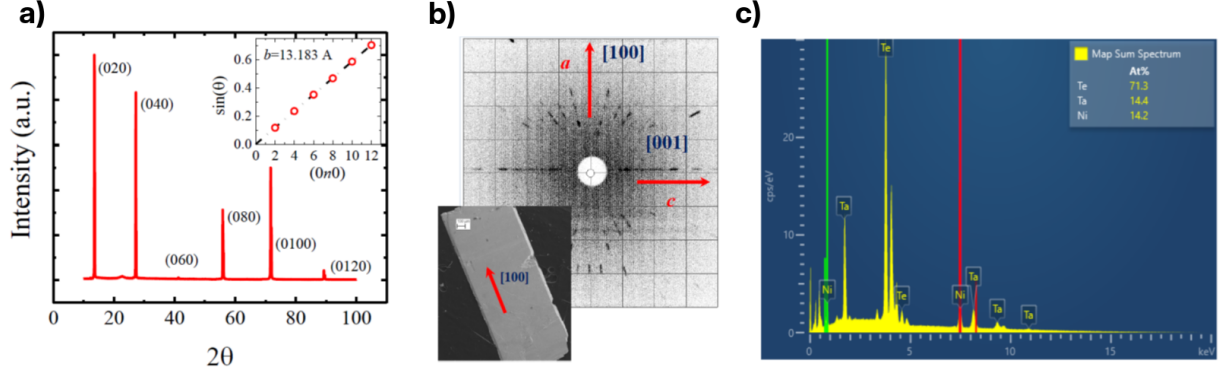


Figure 7. a) Single crystal X-ray diffraction pattern. The inset shows the extracted value of the lattice parameter $b = 13.183 \text{ \AA}$. b) Laue X-ray diffraction pattern, where the inset shows an optical image of a typical crystal. c) The energy-dispersive X-ray spectrum.

Appendix B: Raw Data for Magnetization Measurements

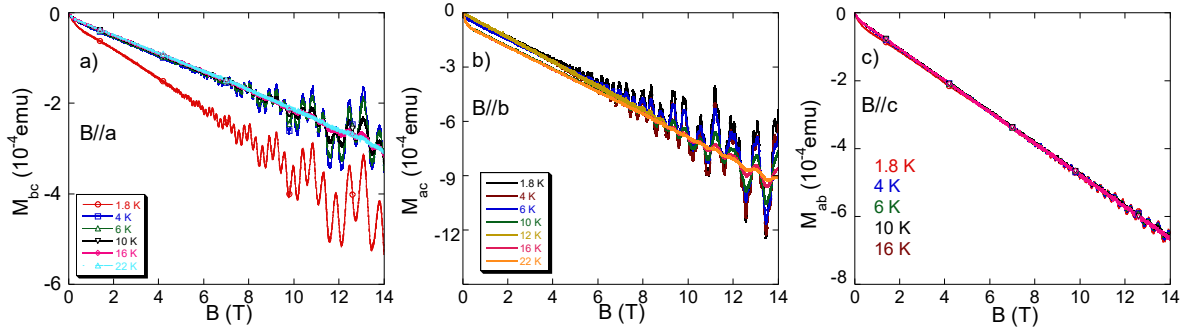


Figure 8. Magnetization for magnetic fields of up to 14 T at various temperatures with the magnetic field applied parallel to the crystallographic a) a -axis, b) b -axis and c) c -axis.

Appendix C: Analysis of Magnetization Measurements

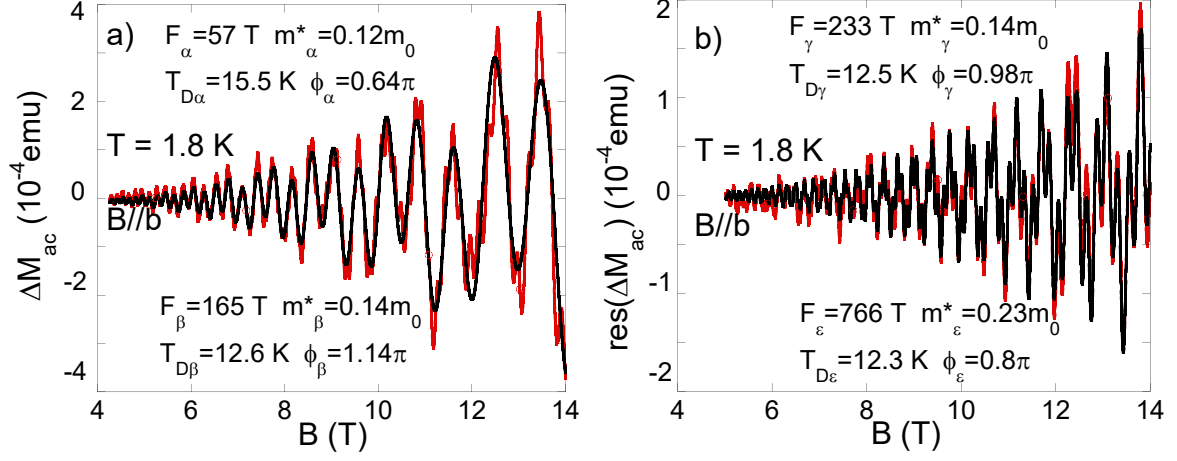


Figure 9. a) The oscillatory component of the isothermal magnetization ΔM after subtracting a diamagnetic background. The magnetic field is applied parallel to the crystallographic b axis. The black lines show the fit of the oscillation pattern assuming two bands. b) Two-band LK formula fit to the residual after subtracting the first two-band fit from the data in a). This result implies that the raw data can best be fitted with a four-band LK formula.

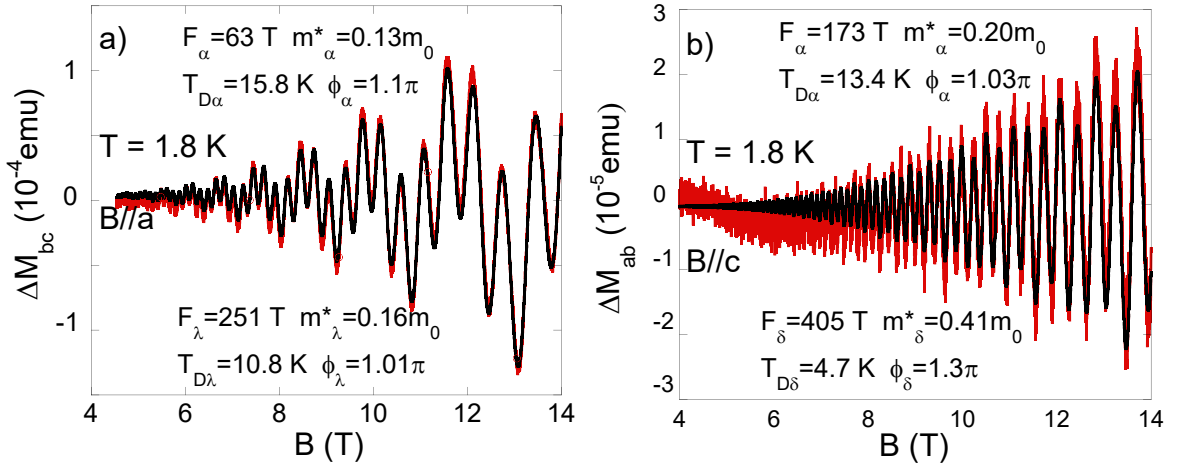


Figure 10. The oscillatory components of the isothermal magnetization ΔM after subtracting the diamagnetic background. The magnetic field is applied parallel to the crystallographic a) a , and b) c axis. The black lines show the fit of the oscillation pattern assuming two bands. In b) another two-band fit was performed after subtracting the first two-band fit from the raw data similar to Figure 9 (not shown here) to obtain values for F_τ and F_η . However, the resolution was too low to extract meaningful information about the phase shift.

Appendix D: Raw Data for Magnetic Torque Measurements

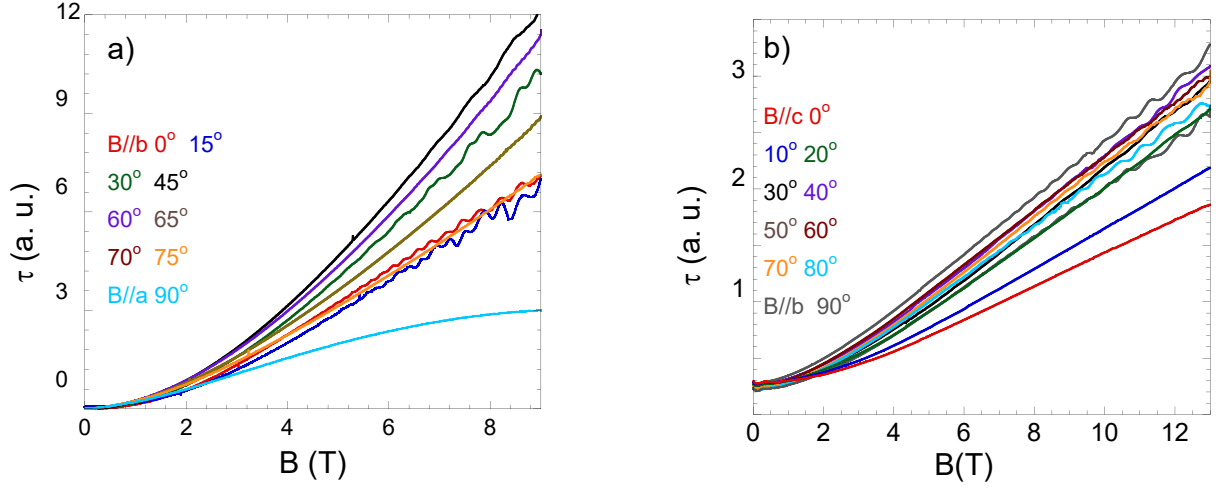


Figure 11. a) The magnetic field sweeps of magnetic torque at various angles at 1.8 K a) for $B \parallel a$ - b plane, and b) for $B \parallel b$ - c plane.

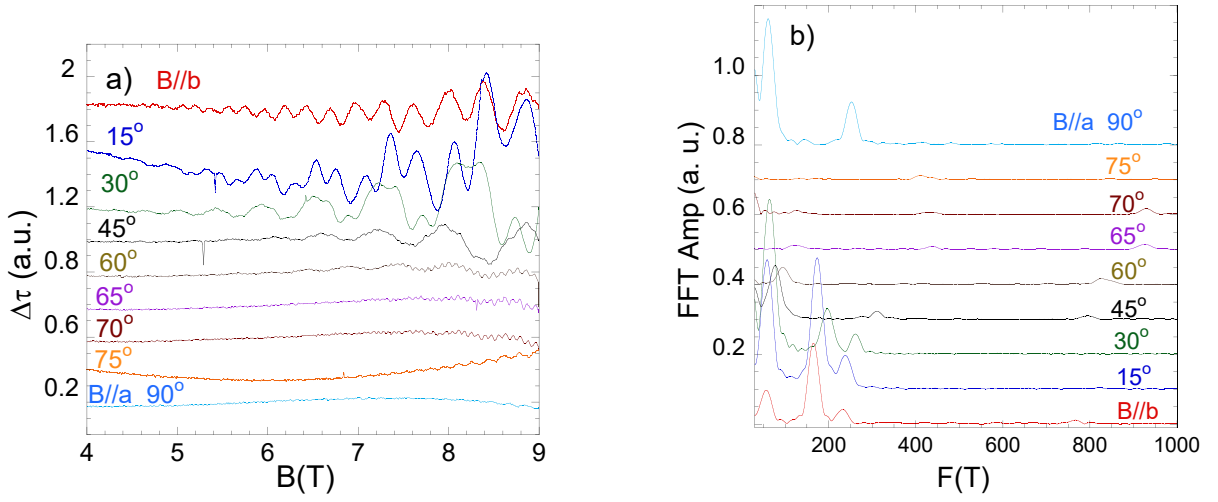


Figure 12. a) Background subtracted magnetic torque data for $B \parallel a$ - b plane at 1.8 K and in the magnetic field range from 4 T up to 9 T. b) Corresponding FFT spectra.

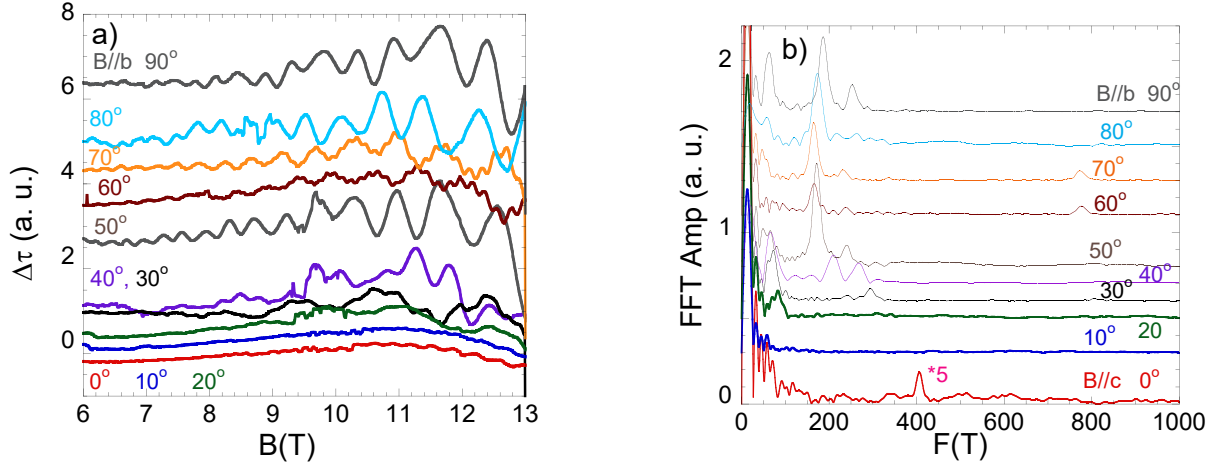


Figure 13. a) Background subtracted magnetic torque data for $B \parallel b$ - c plane at 1.8 K and in the magnetic field range from 6 T up to 13 T. b) Corresponding FFT spectra.

Appendix E: Raw Data for Transport and Thermopower

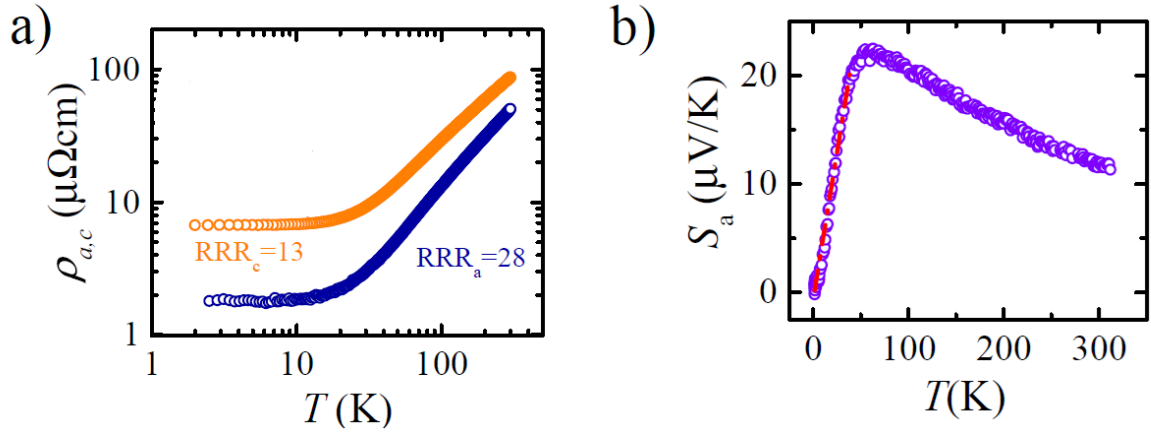


Figure 14. a) Temperature dependence of the resistivity with $\text{RRR}_a = 28$ and $\text{RRR}_c = 13$ in the temperature range from 300 K down to 2 K. b) Temperature dependence of the Seebeck coefficient along the a -axis in the temperature range from 300 K down to 2 K.

Appendix F: Raw Data for Magnetoresistance

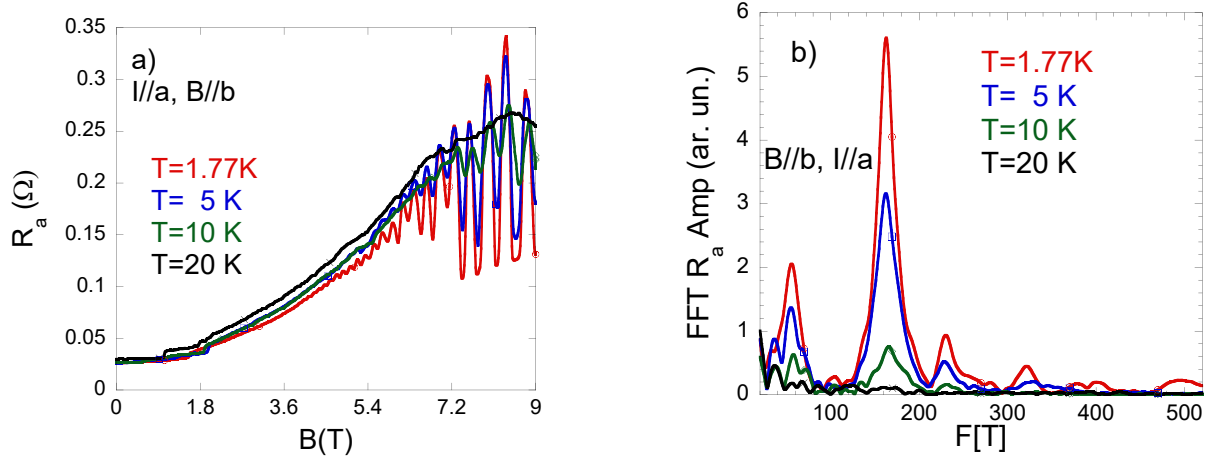


Figure 15. a) Magnetic field sweeps of the resistance at various temperatures between 1.77 K and 20 K. b) Corresponding FFT spectra generated from the raw data between 6 T and 9 T.

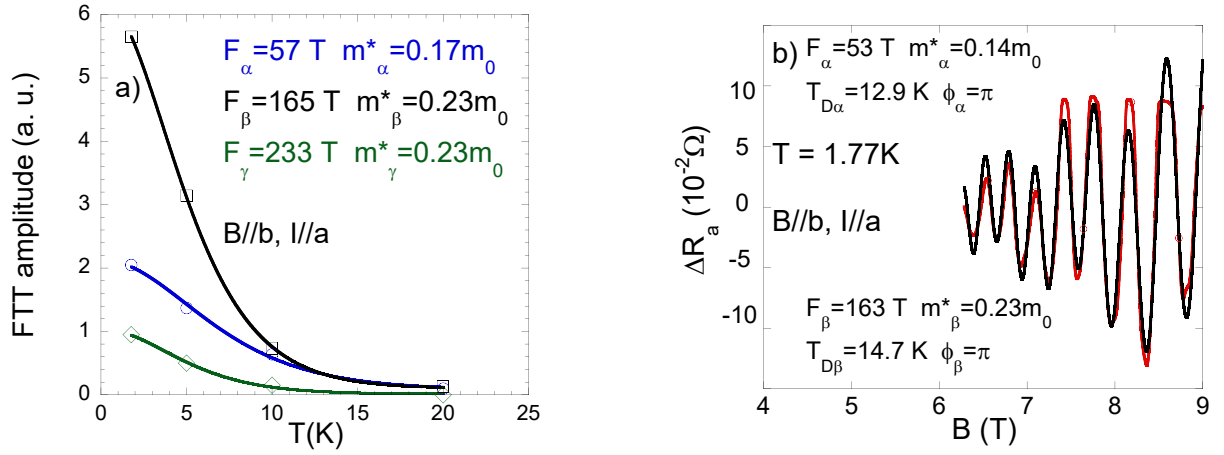


Figure 16. a) The fits of the temperature damping factor R_T in the LK formula to the FFT amplitudes. b) The oscillatory component of the background-subtracted resistance and corresponding fit at $T = 1.77$ K.